Composites Part B 226 (2021) 109352

Contents lists available at ScienceDirect

Composites Part B

journal homepage: www.elsevier.com/locate/composites

Experimental investigation of the path-independent fracture of composites

S. Goutianos

Department of Manufacturing and Civil Engineering, Norwegian University of Science and Technology, Teknologivegen 22, 2815 Gjøvik, Norway

ARTICLE INFO

Keywords:
Mixed mode fracture
J integral
Fracture resistance
Cohesive law

ABSTRACT

Cohesive zone modelling is the main tool to solve the problems of crack initiation and growth, and therefore several mixed-mode cohesive laws are being developed. The majority of the cohesive laws are path independent because this property offers several advantages. However, there has been no experimental evidence of path-independent fracture. Within linear elastic fracture mechanics, path independence is a prerequisite, but not in problems with a large fracture process zone. In this study, it was demonstrated experimentally that path independence applies, to a certain degree, to unidirectional composites with large-scale fibre bridging. Thus, path-independent mixed-mode cohesive laws, preferably derived from a potential function, can be used to describe fracture for this class of materials.

1. Introduction

The concept of describing fracture by a traction–separation law or a cohesive law was first introduced by [1] and [2]. Then, Needleman [3] incorporated a mode I cohesive zone model in a continuum mechanics finite-element model. Needleman [4] and Xu and Needleman [5] extended the concept of cohesive laws to account for mixed-mode fracture, where the fracture process zone is subjected to normal and tangential separations. Since then, cohesive-based finite-element modelling has been the main technique for analysing fracture problems involving crack initiation and growth e.g. [6–9].

Because the fractures in many structures or components — in particular, layered structures, such as composite or sandwich structures — comprise a mixed mode, a large number of mixed-mode partition theories e.g. [10,11] and mixed-mode cohesive laws are being continuously developed. The mixed-mode cohesive laws can be classified into different categories depending on their characteristics, as described by Goutianos and Sørensen [12]. A fundamental property is path independence [4,13–17] - for example, mixed-mode cohesive laws derived from a potential function are path independent. For path-independent mixed-mode cohesive laws, the work of the cohesive traction depends only on the normal and tangential separations and not on the opening history, as schematically shown in Fig. 1a and in Fig. 1b with solid lines. If three loading paths (p_o, p_1 and p_2) are considered between points O and A, then the mixed-mode fracture energy is independent of the loading history (or loading path). For mixed-mode cohesive laws, which are path dependent [8,18,19], the mixed-mode fracture energy depends on the loading history, as shown in Fig. 1b with dashed lines. The energy dissipation in the fracture process zone is the same for path-dependent and path-independent mixed-mode cohesive laws only when the loading is proportional (path p_o in Fig. 1). Typically, a mixed-mode cohesive law is path dependent if it cannot be derived from a potential function.

Path independence is a necessary characteristic for mixed-mode cohesive laws when modelling fractures in the framework of linear elastic fracture mechanics (LEFM), which is an energy-based approach to fracture. Within LEFM, the criterion for crack growth under mixed mode (plane stress) is

$$\mathcal{G}(\tilde{\psi}) = \mathcal{G}_c(\tilde{\psi}) \tag{1}$$

where $\mathcal{G}_c$ is the critical energy release rate or fracture energy and $\mathcal{G}$ is the energy release rate given by

$$\mathcal{G}(\tilde{\psi}) = \frac{K_I^2 + K_{II}^2}{E} \tag{2}$$

Within LEFM, $\mathcal{G}$ is equal to J in Fig. 1. Moreover, $\mathcal{G}_c$ is a function of the phase angle, $\tilde{\psi}$, of the stress intensity factors K_I and K_{II}, which is also called 'mode mixity' [20,21]. Under LEFM, $\tilde{\psi}$ equals the phase angle of the crack tip stresses, ψ. Eqs. (1) and (2) are independent of the loading history, i.e., the onset of fracture occurs at the same value of $\mathcal{G}_c$ irrespective of whether K_I and K_{II} are increased proportionally.

In many cases where it is known that fracture involves strong history-dependent fracture mechanisms, such as plastic deformation or frictional sliding [19], then it is necessary to use path-dependent mixed-mode cohesive laws.

Several modern materials, e.g., composites and adhesive joints, are tough, presenting a large-scale fracture process zone; thus, LEFM, in many cases, cannot be used. Therefore, it is unclear whether path-independent or path-dependent cohesive laws should be used. In general, it is preferable to use path-independent mixed-mode cohesive

E-mail address: stergios.goutianos@ntnu.no.

https://doi.org/10.1016/j.compositesb.2021.109352
Received 4 April 2021; Received in revised form 26 June 2021; Accepted 23 September 2021
Available online 6 October 2021

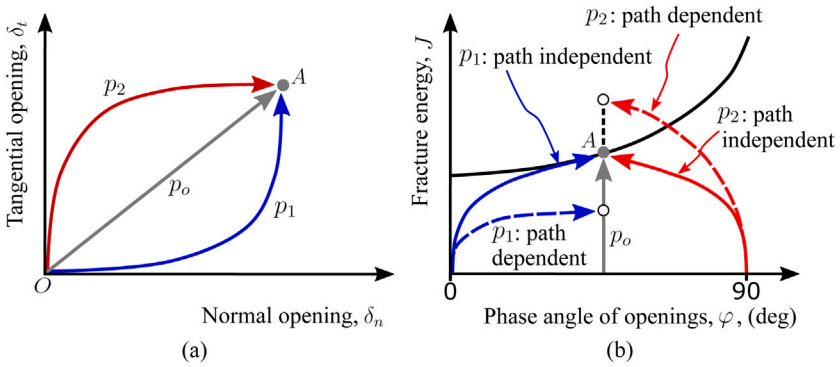

Fig. 1. (a) Proportional loading path (p_o) and nonproportional loading paths (p_1 and p_2), (b) Path independent (solid lines) and path dependent (dashed lines) mixed-mode fracture energy.

laws, even under nonproportional loading [9]. For path-dependent cohesive laws, every possible loading path would result in a different fracture energy, as shown in Fig. 1b. A consequence of this is that these cohesive laws should be able to predict the correct energy dissipation along different loading paths. This could be done by using mixed-mode cohesive laws based on micromechanical models, which include path-dependent failure mechanisms or based on mixed-mode fracture experiments along different loading paths. Without such models or experiments, the use of path-dependent mixed-mode cohesive laws will probably yield incorrect predictions, e.g., it will be uncertain whether the correct energy is dissipated from point O to point A in Fig. 1. However, the use of path-independent mixed-mode cohesive laws ensures that the prescribed energy is dissipated between points O and A. However, for most cases, there is no experimental evidence showing that fracture is path independent or path dependent. The lack of such experiments mainly results from the experimental difficulties in applying nonproportional loading paths.

Thus, the aim of this study was to investigate whether path-independent mixed-mode fracture is a reasonable assumption for materials that exhibit a large-scale fracture process zone. The study was limited to composite materials where the large-scale fracture process zone is caused by fibres bridging the crack faces at the crack tip wake. It should be noted that such composite materials exhibit a relatively large scatter in fracture resistance and the scatter increases with increasing the mode II component. For unidirectional fibre composites similar to the ones used in the present work, steady-state fracture resistance differences in the order of 0.3-0.5 kJ/m^2 or larger than 2.0 kJ/m^2 as the mode mixity increases to near mode II are typical [22–24]. Therefore, such experimental evidence, as in the present work, can justify the use of path-independent mixed-mode cohesive laws for fracture simulations of composite materials and structures, considering the natural variation in the fracture resistance. In addition, it demonstrates that it is sufficient to perform mixed-mode fracture experiments under proportional loading.

The remainder of this paper is organised as follows. First, the experimental procedure is presented. Then, the experimental results are presented. Finally, the obtained results and their implications are discussed.

2. Experimental details

2.1. Materials and specimen manufacturing

A laminate was manufactured by vacuum infusion of an epoxy resin into layers of noncrimp unidirectional E-glass fabrics. A 35- ±15-μm-thick and 60-mm-long perforated release film (Teflon) was placed in the middle of the fabrics along one of the edges of the laminate. The perforated release film (slip foil) was stiff enough to avoid being wrinkled or folded and it acted as a crack starter. Subsequently, the epoxy resin was infused. The use of a perforated film as crack starter ensured that there were no dry spots after the infusion. The curing cycle was 19 h at 40 ° C, followed by 5 h at 75 ° C. The Young's modulus in the fibre direction, E_{11}, was approximately 38 GPa. Double cantilever beam (DCB) specimens were subsequently cut from the laminate for mixed-mode fracture experiments using the fixture shown in Fig. 2a. The specimen length, L, was 500 mm, the width B was 30 mm, and the height, $2H$, was 14 mm (see Fig. 2b). Steel parts (tabs), which made it possible to mount the DCB specimens on the test fixture (Fig. 2a), were fitted to the DCB specimens with screws and an epoxy glue (Fig. 2c). Pins were placed in the neutral axis of each beam at the end of the slip foil, as shown in Fig. 2b.

2.2. Loading arrangement and instrumentation

The fixture that was used to apply pure bending moments, M_1 and M_2, using two transverse arms [22,25] is schematically shown in Fig. 2a. The two moments are $M_1 = P\ell_1$ and $M_2 = P\ell_2$, where the force P in the steel wire is constant. Thus, the moment ratio M_1/M_2 is controlled by changing the length of the two transverse (moment) arms ℓ_1 and ℓ_2. As the lower beam (see Fig. 2a) moves downward, the force P increases; thus, the two moments also increase, i.e., applied rotations are applied in practice. The force is measured by two load cells, and the average value is used to calculate M_1 and M_2. The experiments were conducted at a constant displacement rate of the lower beam of 5 mm/min, and the force data were acquired at a frequency of 20 Hz. Details regarding considerations to minimise the errors in the applied moments e.g. due to friction in the rollers can be found elsewhere [25].

An extensometer (Instron, type 2620–602), with a range of ±2.5 mm, was mounted in the pins, as shown in Fig. 2c. The extensometer was free to rotate and, therefore, measure the magnitude of the crack opening displacement, δ_m^*, at $x_1 = 0$ mm under the assumption that the elastic strain in the beams between the neutral axes and the crack surfaces is negligible. The data from the extensometer were also acquired at a frequency of 20 Hz.

As shown in Fig. 2a, acoustic emission (AE) sensors were also mounted on the specimen surface to record the acoustic activity during fracture and a coarse speckle pattern on the side surface for digital image correlation (DIC). However, the AE and DIC data are not shown in the present work. All the tests were video recorded with the camera facing the DCB specimens in the x_1-x_2 plane (see Fig. 2).

3. J-Integral evaluation and loading procedure

3.1. J-Integral evaluation

For a DCB specimen loaded with uneven bending moments, the fracture energy can be calculated by evaluating the J-integral [26] along the external boundaries of the specimen [22,25]. For an orthotropic

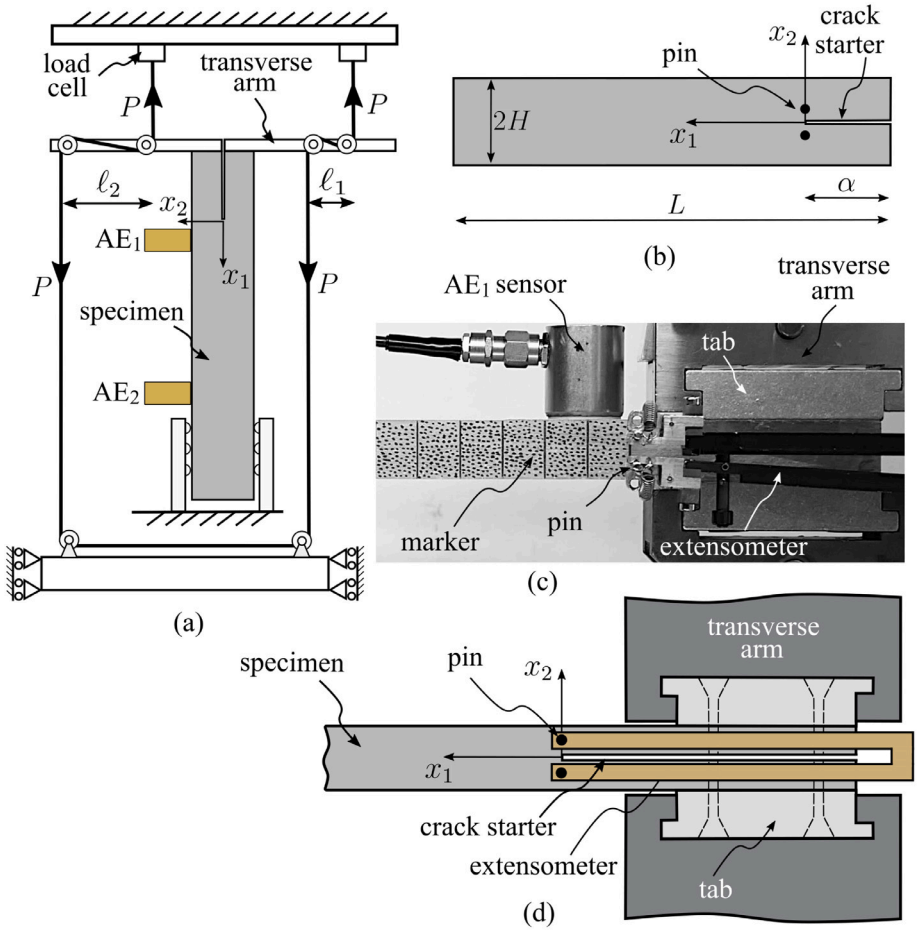

Fig. 2. (a) Schematic illustration of test fixture to apply pure uneven bending moments using a wire and rollers, (b) the double cantilever beam (DCB) specimen showing the position of the slip foil and the pins, (c) photograph of a DCB specimen showing the extensometer and the fixation to the transverse arms and (d) schematic illustration of (c).

specimen and under plane strain, the J-integral along the external boundaries is given by

$$J_{ext} = (1-\nu_{12}^2)\frac{21(M_1^2+M_2^2)-6M_1M_2}{4B^2H^3E_{11}}, \text{ for } |M_1| < M_2 \tag{3}$$

where M_1 and M_2 are measured during the experiment, and ν_{12} is the Poisson ratio with an assumed value of 0.3. The value of ν_{12} has a minor effect on J_{ext}. Eq. (3) is valid for both small and large-scale fracture problems. Under LEFM, the mode mixity for an orthotropic specimen is [25]

$$\tilde{\psi}(\lambda, M_1/M_2) = \tan^{-1}\left\{\lambda^{-1/4}\frac{\sqrt{3}}{2}\left(\frac{1+M_1/M_2}{1-M_1/M_2}\right)\right\} \tag{4}$$

where $\lambda = E_{22}/E_{11}$ [27].

The mode mixity, $\tilde{\psi}$, is used occasionally in the next section for the different DCB specimens together with the moment ratio M_1/M_2, which is the appropriate parameter for problems with large-scale fracture process zones. Table 1 lists the moment ratios used in the present study and the associated nominal mode mixities.

Table 1
Relationship between the mode mixity $\tilde{\psi}$ and the moment ratio M_1/M_2.

Mode mixity, $\tilde{\psi}$ (deg)	Moment ratio, M_1/M_2 (-)
0.0	−1.0
41.0	0.0
58.0	0.299
88.0	0.943

3.2. Loading procedure

Fig. 3 shows the fracture resistance, J_R, as a function of δ_m^* for a DCB specimen monotonically loaded to steady-state fracture in pure mode I. At a certain load level (state a_1), a crack is initiated at the root of the initial notch. By further increasing the load, the crack tip extends, and, at the wake of the crack tip, a fracture process zone (FPZ_b) develops (state a_2 in Fig. 4a). In composites, the FPZ_b typically consists of fibres bridging the crack faces and together with the crack tip fracture process zone (FPZ_c) constitute the entire fracture process zone (FPZ), with a length typically of several millimetres. If the FPZ is small compared to the stress field controlled by the stress intensity factors K_I and K_{II} (Eq. (1)), LEFM applies. The K-dominant zone depends on the specimen geometry and for DCB specimens is rather small [10,28]. For a homogeneous DCB specimen, the size of the K-dominant zone, defined as a circle with the crack tip at its centre and radius r_K, is approximately $r_K = 0.01H \approx 70$ μm. Therefore, a FPZ in the order of several millimetres is large compared to the K-dominant zone and LEFM is strictly not applicable.

In the case of pure bending moments, as in the present work, the FPZ continues to increase in length until all bridging fibres fail in the region close to the root of the initial notch (state a_3 in Fig. 4a). At this moment, the FPZ is fully developed. By further increasing the applied rotation, the FPZ translates along the specimen length under constant moments without changing its length (state a_4 in Fig. 4a). In practice,

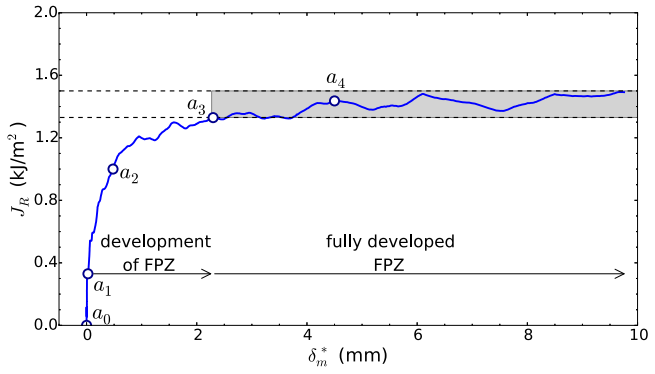

Fig. 3. Fracture resistance, J_R, as a function of the magnitude of end opening, δ_m^*, for a DCB specimen monotonically loaded in pure mode I to steady-state fracture.

owing to material variation along the fracture plane, there is some variation in the steady-state fracture resistance, as can be seen in Fig. 3.

As mentioned in Section 1, it is experimentally difficult to achieve nonproportional loading paths, such as p_1 or p_2 in Fig. 1. For this reason, in the present work, each DCB specimen was loaded with a fixed M_1/M_2 ratio up to a load level high enough to cause crack growth on the order of 20 to 40 mm (state a_2 in Fig. 4a). From the monotonically loaded DCB specimens [29] for the same M_1/M_2 ratio, it was known in advance that, at this load level, the steady-state fracture would not be reached. The length of the FPZ at this point is denoted as ℓ^1_{FPZ}. After the crack grew, the DCB was completely unloaded. The lengths ℓ_1 and ℓ_2 were then changed to have a different M_1/M_2 ratio (Fig. 4b). Upon loading the DCB specimen again, the FPZ developed in a process zone morphology left by the first loading (states b_0 and b_2 in Fig. 4b). As mentioned above, by further increasing the applied rotation, a steady state, J_R^{ss}, is achieved when the bridging fibres fail at the root of the notch (state b_3 in Fig. 4b). Owing to the different moment ratios, the length of the fully developed zone was generally different from the previous loading step. A further increase of the applied rotations caused the FPZ to translate along the specimen length at a constant load (steady-state fracture). The fracture process zone length, when the bridging fibres fail at the crack tip of the first loading step is denoted as ℓ^2_{FPZ}. The crack growth, afterwards, takes place in a virgin material, and there should be no loading history effects. After steady-state crack growth (in most cases, of several millimetres), the specimen was completely unloaded. The experimentally measured steady state fracture resistance in state b_4 is different from J_R^{ss} as it will be shown in the next Section. Its maximum value is denoted as $J_R^{ss,max}$. Both J_R^{ss} and $J_R^{ss,max}$ will be presented. It should be noted that J_R^{ss} differs from $J_R^{ss,max}$ also for the monotonically loaded DCB specimens.

This study focused, in the second loading step, on the fracture response until a steady state was reached because it is in this region that there is an effect from the process zone morphology left by the first loading. Because it was not sufficiently accurate to determine when the steady-state was reached by curves, as shown in Fig. 3, video recording was used to identify when the bridging fibres failed at the root of the initial notch as shown for example for a monotonically loaded DCB specimen in Fig. 5. The frames from (a) to (d) correspond to increasing load. It can be seen that at a certain load the bridging fibres fail at the root of the notch (Fig. 5d). It should be noted that this technique involves to a certain degree subjective judgment of the load level or the end opening where the bridging fibres fail at the root of the notch. However, this uncertainty is not critical since the error for example in determining the critical end opening is in the order of microns.

Because the DCB specimens were transparent, the crack front (plane x_1-x_3) was clearly visible during loading and unloading. The crack front in all cases was nearly straight. The delamination/crack tip, along x_1 was at the same location on both sides of the DCB specimens.

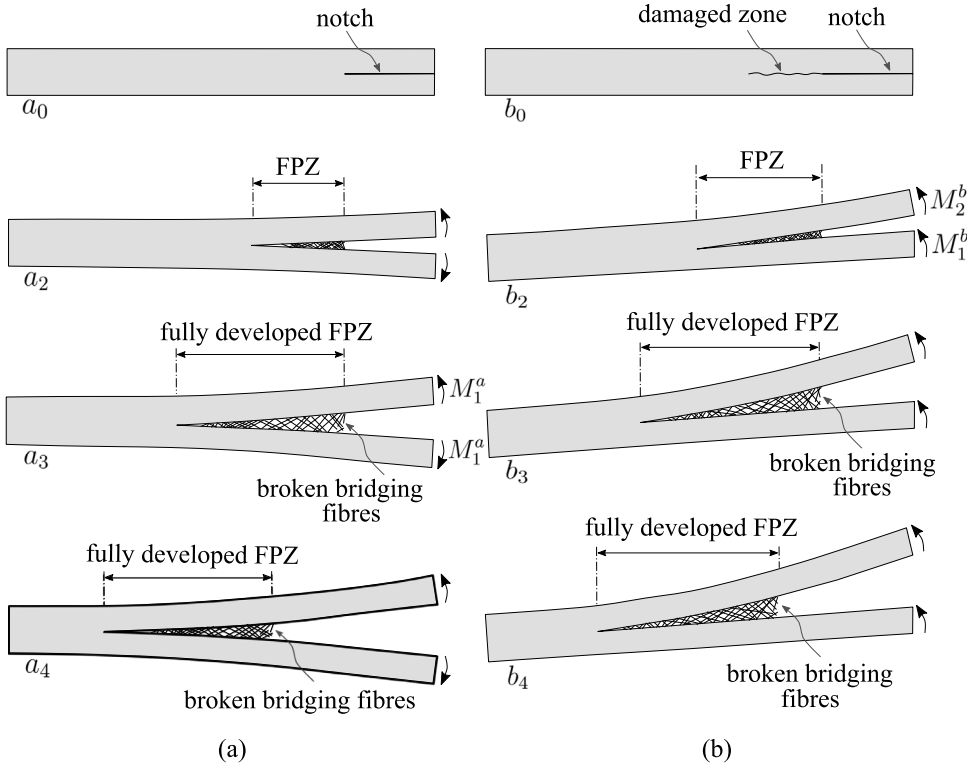

Fig. 4. Fracture process zone (FPZ) development in a DCB specimen loaded with pure bending moments: a) fracture initiates from a notch and (b) fracture extends from a damaged region.

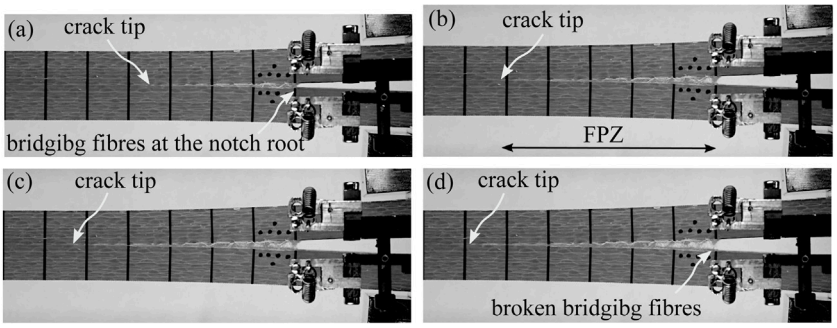

Fig. 5. Determination of the load level and of the end opening where the bridging files fail at the root of the notch using the frames from video recording. The load level increases from frame (a) to frame (d).

Table 2
Loading details and fracture resistance in the first (1) and in the second (2) loading steps for the nonproportionally loaded DCB specimens: the specimens are completely unloaded after the first loading step.

No	1st loading (1) M_1/M_2 (-)	J_R (N/m)		2nd loading (2) M_1/M_2 (-)	J_R^{ss} (N/m)	$J_R^{ss,max}$ (N/m)
1	−1.0	952.5	→	0.0	2627.9	3423.8
2	0.943	4131.4	→	0.0	2669.0	3832.6
				Average	2648.5 ± 29.1	3628.2 ± 289.1
3	0.0	2477.4	→	−1.0	1594.2	2812.2
4	0.299	2408.8	→	−1.0	1032.4	1053.7
5	0.943	4142.9	→	−1.0	916.0	1091.4
				Average	1180.9 ± 362.7	1652.4 ± 1004.6
6	−1.0	969.4	→	0.943	7781.8	8617.4
7	0.0	2091.7	→	0.943	5246.0	5682.4
8	0.299	2820.8	→	0.943	7970.6	8746.1
				Average	6999.5 ± 1521.5	7682.1 ± 1733.0

4. Results

4.1. Steady-state fracture resistance

Fig. 6 shows the steady-state fracture resistance of the DCB specimens, which were subjected to two loading steps with different moment ratios at each step, as described in Table 2. The data are plotted as coloured circle symbols and refer to the second loading step. More specifically, the steady-state fracture resistance values, J_R^{ss}, correspond to the fracture resistance when the bridging fibres fail at the root of the initial notch (state b_3 in Fig. 4b) in the second loading step. These nonproportional-loading steady-state fracture resistance values are compared with the steady-state fracture resistance of DCB specimens continuously loaded up to steady-state fracture (monotonic, proportional loading, and one loading step), which are plotted as square symbols. It is clear that both sets of DCB experiments, proportional (one loading step) and nonproportional (two loading steps) loading, yield the same steady-state fracture resistance within experimental tolerance.

The results of Fig. 6 for the nonproportionally loaded DCB specimens are also given in Table 2, which includes the maximum fracture energies, J_R, attained in the first loading step prior to unloading. The maximum steady-state fracture resistance values obtained during the second loading step, $J_R^{ss,max}$, are also given. In most cases, J_R^{ss} and $J_R^{ss,max}$ (always referring to the second loading) are comparable. For specimen 3 and to a lesser extent for specimens 1 and 2, $J_R^{ss,max}$ is higher than J_R^{ss}. For comparison purposes, the maximum steady-state fracture resistance values of the monotonically loaded DCB specimens are given in Table 3.

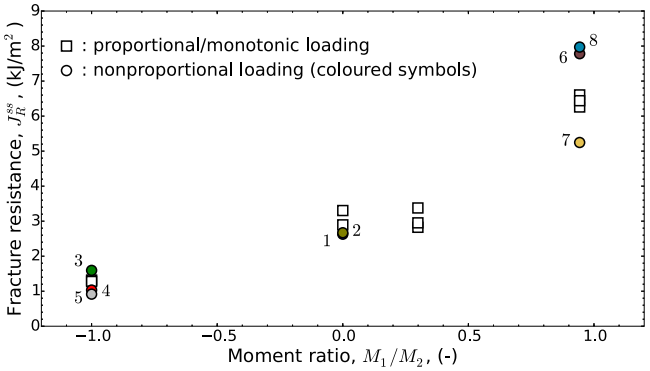

Fig. 6. Steady-state fracture resistance, J_R^{ss}, as a function of the moment ratio M_1/M_2 for specimens loaded proportionally/monotonically to steady-state and specimens loaded in two steps with different moment ratios, nonproportional loading (see Table 2). (For interpretation of the references to colour in this figure legend, the reader is referred to the web version of this article.)

Table 3
Loading details and fracture resistance for the proportionally loaded DCB specimens (average values from 3 specimens).

M_1/M_2 (-)	J_R^{ss} (N/m)	$J_R^{ss,max}$ (N/m)
−1.0	1213.1 ± 143.8	1297.7 ± 202.1
0.0	2982.0 ± 288.8	3883.0 ± 646.3
0.299	3063.9 ± 350.4	3141.7 ± 367.2
0.943	6601.8 ± 111.2	6687.3 ± 571.6

4.2. Fracture resistance curves

Fig. 7a shows the fracture resistance curve for DCB specimen 1 (Table 2) loaded in pure mode I up to δ_m^* of approximately 1 mm. The fracture response follows the behaviour of two DCB specimens monotonically loaded to steady-state fractures [29]. At $\delta_m^* \approx 1$ mm, the length of the FPZ, ℓ_{FPZ}^1, is approximately 21.5 mm and corresponds to the damage state a_2 in Fig. 4, e.g., a not fully developed FPZ. Then, the specimen is completely unloaded. When the load drops to zero, δ_m^* is approximately 0.05 mm.

In the second loading step (Fig. 7b), the specimen is loaded with a different M_1/M_2 ratio of 0.0, and the response is again compared with two DCB specimens monotonically loaded under the same moment ratio to a steady-state fracture. The response of specimen 1 is initially linear, up to $\delta_m^* \approx 1$ mm, because of the damage induced in the first loading step. As the load is further increased, the crack propagates, and the bridging fibres within the FPZ are subjected to a different mode mixity than that in the first loading step. The damage state b_3, where the bridging fibres fail at the root of the initial notch, is reached at $\delta_m^* \approx$ 3.6 mm. This damage state is reached for approximately the same end opening as for the monotonically loaded specimens (damage state a_3 in Fig. 4). When the applied load is increased further, the crack grows. When δ_m^* is approximately 7.2 mm, the bridging fibres at the end of the FPZ from the first loading step fail. Thus, for δ_m^* between 1 and 7.2 mm, the crack grows in a region damaged during the first loading step, yet the fracture resistance curve of specimen 1 resembles the response of the two monotonically loaded specimens with $M_1/M_2 = 0$.

Fig. 8 is similar to Fig. 7 with the difference that specimen 2 is loaded near mode II in the first loading step. The length of the FPZ induced in this loading step is approximately 34.2 mm. During the second loading step, the response is linear up to a δ_m^* of 1.35 mm. The corresponding J_R value is approximately 1.9 kJ/m^2 and approximately two times lower than the maximum J_R reached in the first loading step before unloading. Similar to Fig. 7b, the bridging fibres fail at the root of the initial notch at the same end opening as for the monotonically loaded DCB specimens with the same moment ratio. Therefore, specimens 1 and 2 reach the damage state b_3 at the same δ_m^* although they have been subjected to a moment ratio in the first loading step that is very different, e.g., mode I versus near mode II.

When steady-state fracture is reached, in the second loading step, there are still fibres bridging the crack faces at the crack tip position of the first loading step. Thus, up to steady-state fracture, there should be an effect from the process zone morphology left from the first loading step if the fracture is path dependent. However, the response of specimen 2 is nearly identical to the response of the two monotonically loaded specimens; thus, it is not influenced by the first loading step.

In Figs. 9–11, the DCB specimens are subjected to a different moment ratio in the first loading step with $M_1/M_2 = 0.0$ ($\tilde{\psi}$ =41°), 0.299 ($\tilde{\psi}$ =58°) and 0.943 ($\tilde{\psi}$ =88°). In the second loading step, all three specimens are loaded in pure mode I, M_1/M_2 =-1.0 ($\tilde{\psi}$ =0°).

Specimen 3 (Fig. 9) is loaded up to a δ_m^* of approximately 1.5 mm, and, as expected, the response follows the response of the monotonically loaded specimens. The corresponding J_R value is approximately 2.5 kJ/m^2. Then, the applied rotation is held fixed until equals 2 mm. Finally, the specimen is unloaded. In the second loading step, the damage state b_3 is reached at the same end opening with the two monotonically loaded specimens loaded in pure mode I. The corresponding fracture resistance value is approximately 1.6 kJ/m^2, which is significantly lower than the fracture resistance, J_R, value reached in the first loading step. However, with further increase of the applied moments, the fracture resistance for specimen 3 deviates from those of the monotonically loaded specimens, and the steady-state fracture resistance is 2.8 kJ/m^2. Thus, up to damage state b_3, it can be argued that there are no loading history effects. Subsequent crack growth, however, appears to be influenced by the first loading step.

For this particular composite material system, [29] found that, under monotonic loading, there is a local maximum in steady-state fracture resistance for a moment ratio of 0.0, which is the moment ratio applied in the first loading step. The monotonically loaded specimens had a long FPZ [29], and the same can be seen for specimen 3 (Fig. 9) with an FPZ length of approximately 80 mm at damage state b_3. Therefore, the behaviour of specimen 3 in Fig. 9b can be attributed to the special fracture behaviour of the selected composite material when M_1/M_2 is 0.0.

Specimen 4 (Fig. 10), however, does not show history loading effects. In the first loading step, the specimen is loaded up to a δ_m^* of 0.8 mm, and the corresponding J_R is 2.3 kJ/m^2. In the second loading step, the crack growth starts at a much lower fracture resistance than in the first loading step, and the response is close to that of the monotonically loaded specimens. The damage state b_3 is reached at a similar end opening (Fig. 10b), and the subsequent fracture resistance curve follows the response of the monotonically loaded specimens. The bridging fibres at the position of the crack tip in the first loading step fail when δ_m^* equals 7.5 mm. Thus, up to this point, the crack grows in a region previously damaged in the first loading step, but no effects are shown in the second loading step. The length of the fully developed FPZ is approximately 61 mm, which is significantly lower than that of the fully developed FPZ length of specimen 3 (Fig. 9).

Specimen 5 (Fig. 11a) is loaded in near mode II up to a δ_m^* of 0.25 mm, and the corresponding J_R value is 4.2 kJ/m^2, almost twice as high as that of specimen 4. In the second loading step, the damage state b_3 is reached at approximately the same end opening as for the monotonically loaded specimens.

Up to a δ_m^* of 7.3 mm, the crack growth occurs in a region that has been damaged in the first loading step, but there is no influence in the response, as Fig. 11b shows. At this point, the length of the fully developed FPZ is almost that of specimen 4 (Fig. 10b). Thus, the responses of specimens 4 and 5 are the same and nearly identical to those of the monotonically loaded specimens. Thus, fracture appears to be path independent.

Figs. 12–14 feature specimens 6–8 (Table 2), which are subjected to different moment ratios in the first loading step and in near mode II in the second loading step.

Specimen 6 is loaded in pure mode I in the first step. Fracture initiates at a J_R of approximately 0.3 kJ/m^2, and the specimen is further loaded up to a δ_m^* of 1.1 mm. The response up to this load follows the responses of two monotonically loaded specimens, and the FPZ length is close to 28 mm. When the specimen is then loaded in near mode II in the second loading step, crack growth does not occur until J_R is approximately 4.4 kJ/m^2, which is significantly higher than the fracture resistance, J_R, values for crack initiation and growth in the first loading step. Moreover, the J_R at which the crack grows in the second step is similar to the corresponding values of the monotonically loaded specimens. When the applied moments (rotations) are increased, the crack grows further, and the damage state b3 is reached at a similar end opening as those of the monotonically loaded specimens (Fig. 12b), although the corresponding J_R value is higher. With a further increase in the loading, the crack continues to grow to a damaged region from the first loading step up to a δ_m^* of 7.7 mm. The overall response of specimen 6 in the second loading step resembles the behaviour of the monotonically loaded specimens up to this point, i.e., the response is not significantly affected by the damage introduced in the first loading step. The fully developed FPZ is approximately 144 mm.

Fig. 13 shows the fracture resistance curves for specimen 7 for the first and second loading steps. In the first step, the moment ratio is 0.0, and the fracture initiates at approximately 1.2 kJ/m^2. The specimen is loaded up to a δ_m^* of 0.85 mm, and the corresponding FPZ length was 23.4 mm. In the second loading step, the crack does not grow until J_R reaches a much higher value of approximately 4.3 kJ/m^2, which is similar to the corresponding values for the monotonically loaded specimens (see Fig. 13b).

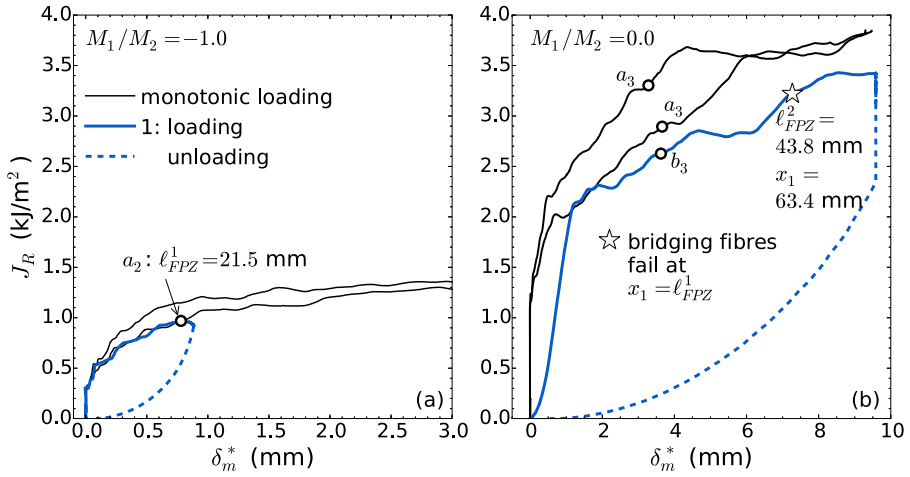

Fig. 7. Fracture resistance as a function of the magnitude of the end opening, δ^*_m, for specimen 1 (Table 2): (a) M_1/M_2 = −1.0 for the first loading, and (b) M_1/M_2 = 0.0 for the second loading — the responses are compared with monotonic (proportional) loading for the same M_1/M_2 ratio, and the damage states a_2, a_3, and b_3 are defined in Fig. 4.

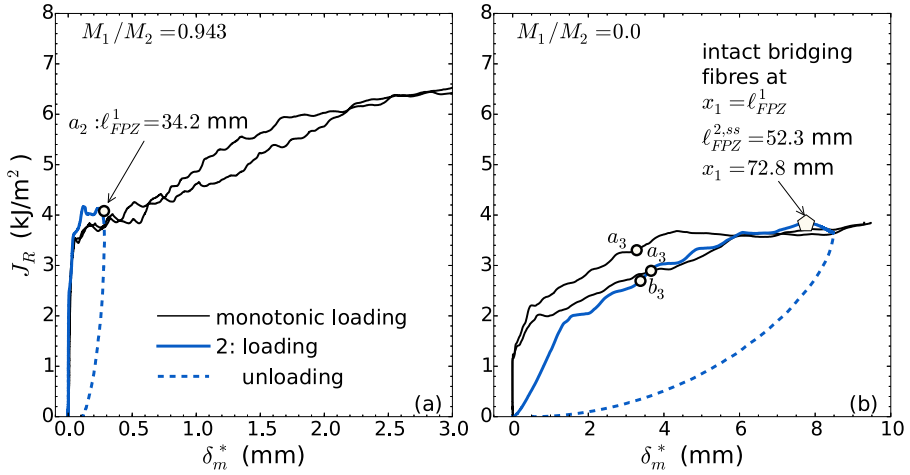

Fig. 8. Fracture resistance as a function of the magnitude of the end opening, δ^*_m, for specimen 2 (Table 2): (a) M_1/M_2 = 0.943 for the first loading, and (b) M_1/M_2 = 0.0 for the second loading — the responses are compared with monotonic (proportional) loading for the same M_1/M_2 ratio, and the damage states a_2, a_3, and b_3 are defined in Fig. 4.

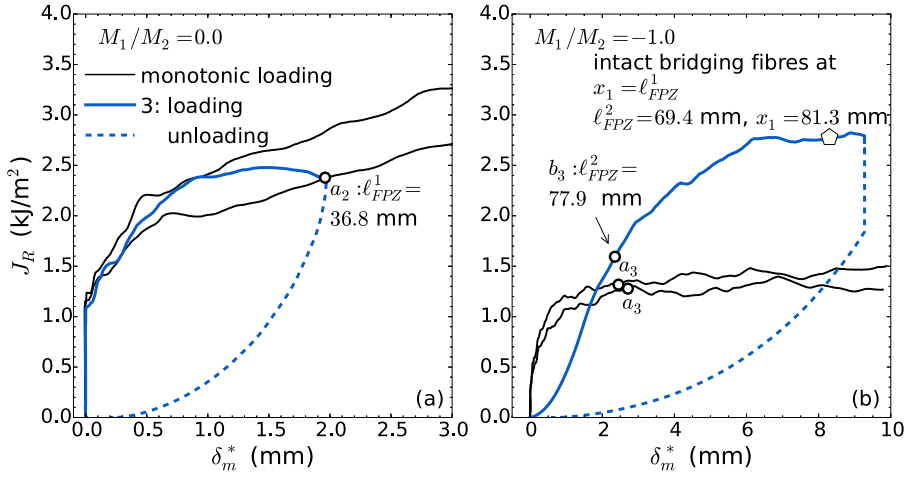

Fig. 9. Fracture resistance as a function of the magnitude of the end opening, δ^*_m, for specimen 3 (Table 2): (a) M_1/M_2 = 0.0 for the first loading, and (b) M_1/M_2 = −1.0 for the second loading — the responses are compared with monotonic (proportional) loading for the same M_1/M_2 ratio, and the damage states a_2, a_3, and b_3 are defined in Fig. 4.

When the loading is increased, crack growth initiates, and growth occurs in the region that was partially fractured in the first step. The bridging fibres fail at the root of the initial notch when δ^*_m is 4.1 mm, which is slightly higher than the corresponding δ^*_m values for the monotonically loaded specimens. Complete fracture at the crack tip of the first loading step occurs when δ^*_m is 6.1 mm. The steady-state fracture

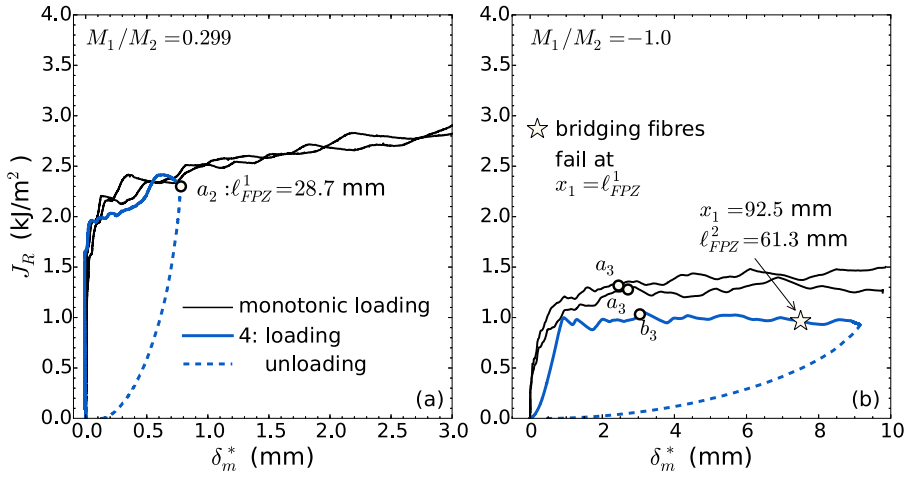

Fig. 10. Fracture resistance as a function of the magnitude of the end opening, δ^*_m, for specimen 4 (Table 2): (a) $M_1/M_2 = 0.299$ for the first loading, and (b) $M_1/M_2 = -1.0$ for the second loading — the responses are compared with monotonic (proportional) loading for the same M_1/M_2 ratio, and the damage states a_2, a_3, and b_3 are defined in Fig. 4.

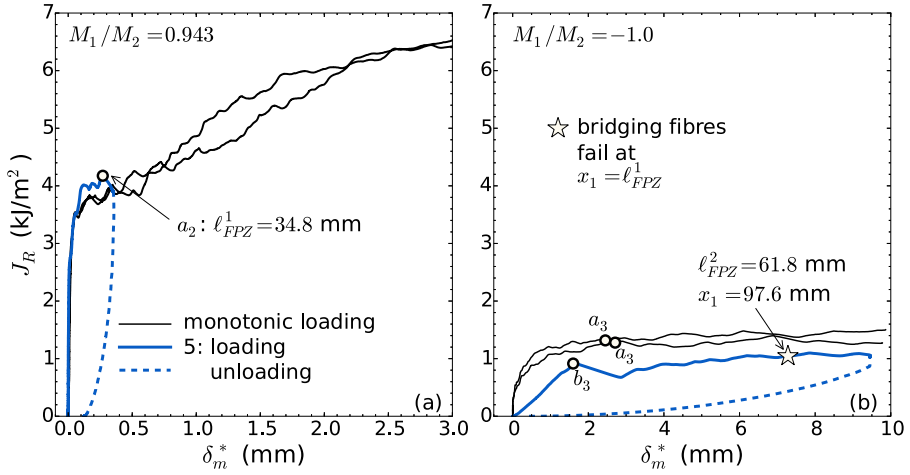

Fig. 11. Fracture resistance as a function of the magnitude of the end opening, δ^*_m, for specimen 5 (Table 2): (a) $M_1/M_2 = 0.943$ for the first loading, and (b) $M_1/M_2 = -1.0$ for the second loading — the responses are compared with monotonic (proportional) loading for the same M_1/M_2 ratio, and the damage states a_2, a_3, and b_3 are defined in Fig. 4.

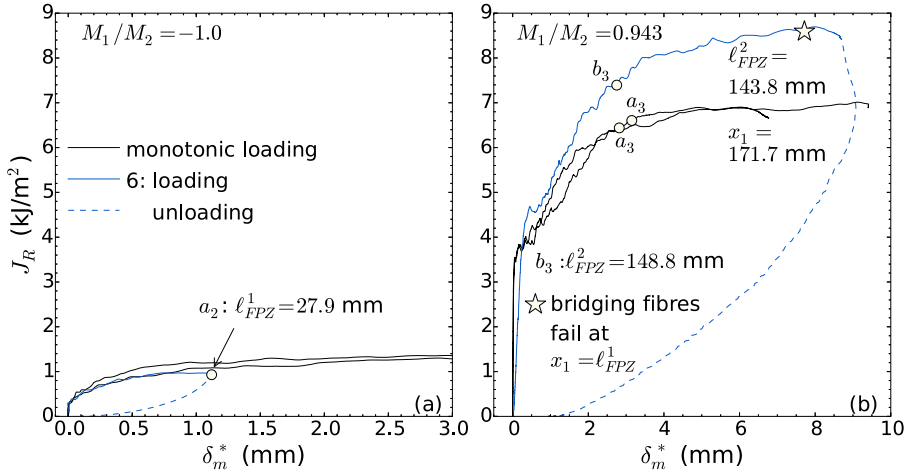

Fig. 12. Fracture resistance as a function of the magnitude of the end opening, δ^*_m, for specimen 6 (Table 2): (a) $M_1/M_2 = -1.0$ for the first loading, and (b) $M_1/M_2 = 0.943$ for the second loading — the responses are compared with monotonic (proportional) loading for the same M_1/M_2 ratio, and the damage states a_2, a_3, and b_3 are defined in Fig. 4.

resistance is lower than that of the monotonically loaded specimens, but this difference is typical for fracture mechanics experiments. It is interesting that the FPZ, when the damage state b_3 is reached, is approximately 151 mm and then reduces to 130 mm.

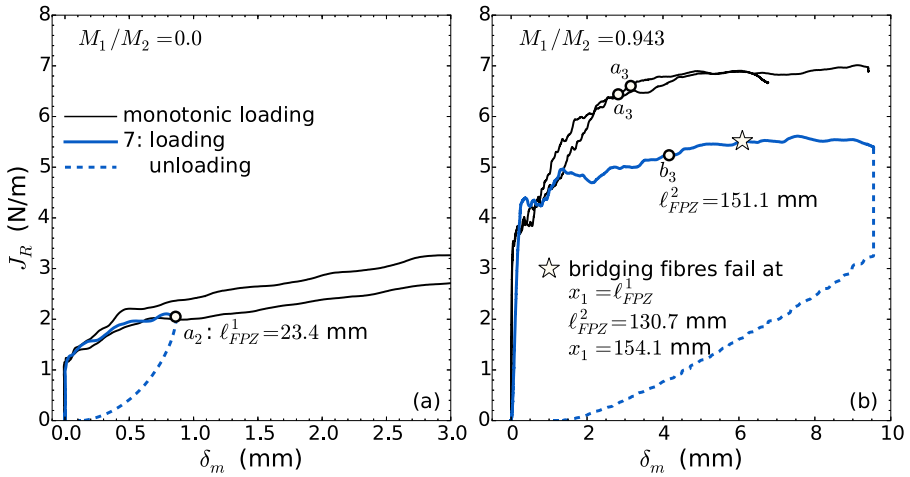

Fig. 13. Fracture resistance as a function of the magnitude of the end opening, δ_m^*, for specimen 7 (Table 2): (a) M_1/M_2 = 0.0 for the first loading, and (b) M_1/M_2 = 0.943 for the second loading — the responses are compared with monotonic (proportional) loading for the same M_1/M_2 ratio, and the damage states a_2, a_3, and b_3 are defined in Fig. 4.

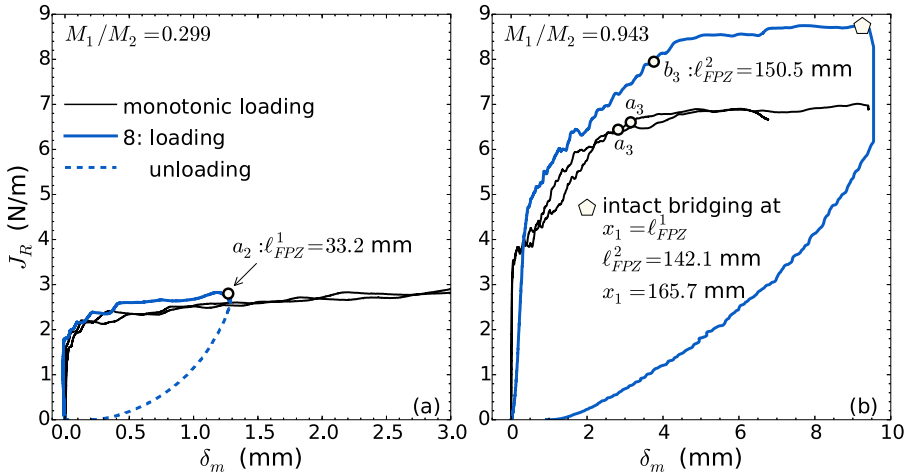

Fig. 14. Fracture resistance as a function of the magnitude of the end opening, δ_m^*, for specimen 8 (Table 2): (a) M_1/M_2 = 0.299 for the first loading, and (b) M_1/M_2 = 0.943 for the second loading — the responses are compared with monotonic (proportional) loading for the same M_1/M_2 ratio, and the damage states a_2, a_3, and b_3 are defined in Fig. 4.

Specimen 8 (Fig. 14) is first loaded with a moment ratio of 0.299. During this step, the fracture initiates at a J_R of 1.8 kJ/m^2, and the specimen is further loaded up to a δ_m^* of 1.25 mm. In the second loading step, crack growth occurs at a J_R of 4.6 kJ/m^2, although, in the first step, an FPZ of 33.2 mm developed at much lower J_R values. The damage state b_3 is reached at the same end opening as the monotonically loaded specimens. When the applied moments increase further, the crack continues to grow until the specimen is unloaded without complete failure of the bridging fibres at the final location of the crack tip in the first loading step. Thus, the entire crack growth should be influenced by the damage of the first loading step as it occurs in a damaged region. However, the fracture resistance curve is similar to that of the monotonically loaded specimens, indicating that the fracture is path independent. The length of the fully developed FPZ is nearly equal to that of specimen 6 (Fig. 12).

5. Discussion

5.1. Path-independent fracture

It is sometimes argued that the damage in the FPZ is irreversible, justifying the use of path-dependent cohesive laws [19]. Although this may be true for certain cases, it is not in general true, as shown in the present work. The results of the previous section show that the fracture of unidirectional composite materials with large-scale fibre bridging at the wake of the crack tip, i.e., large fracture process zone/nonlinear fracture mechanics, is approximately path independent, although the damage is irreversible. The dissipated energy, calculated using the J-integral, is found to be approximately the same along different loading paths, even when extreme loading paths are used. This is an important finding because the use of mixed-mode cohesive laws derived from a potential function is widespread, and the present work provides experimental evidence of the justification of using these cohesive laws to model mixed-mode fractures under arbitrary loading paths. As mentioned in Section 1, one major disadvantage of using path-dependent cohesive laws is that a significantly larger number of experiments would be required to describe such cohesive laws properly. Furthermore, such experiments, i.e., loading at the load path with changing mode mixity, are difficult to perform. This is the reason why most fracture tests are conducted under proportional loading. The present work shows that, for unidirectional composites, it is a good approximation to assume that fracture is path independent; therefore, path-independent cohesive laws derived from proportionally loaded fracture experiments can describe a unique mixed-mode failure envelope.

The current work focuses on composite materials and, in particular, unidirectional composites. Similar experiments should be performed for other material types to determine whether the assumption of path-independent fracture is reasonable.

5.2. Validity of the J-integral approach

Owing to experimental difficulties in applying different loading paths, the approach used in the present work of complete specimen unloading before changing the applied mode mixity, in principle, invalidates the use of the J-integral. However, it is shown that, in the case of large-scale fibre bridging, the J-integral approach can still be used. A physical explanation is that, in the case of fibre bridging, during unloading, there is no further damage accumulation.

6. Concluding remarks

The most commonly used mixed-mode cohesive laws are based on a potential function and, therefore, are path independent. This characteristic agrees with the premises of LEFM. However, for fracture problems with large-scale fracture process zones, as in the case of composite materials, path independence has not previously been tested experimentally. In the present work, it was experimentally shown that, for unidirectional composites with a large-scale fracture process zone, path independence is a reasonable assumption. Therefore, path-independent mixed-mode cohesive laws, e.g., ones derived from a potential function, could be used instead of path-dependent cohesive laws.

CRediT authorship contribution statement

S. Goutianos: Conception and design of study, Acquisition of data, Analysis and/or interpretation of data, Writing – original draft, Writing – review & editing.

Declaration of competing interest

The authors declare that they have no known competing financial interests or personal relationships that could have appeared to influence the work reported in this paper.

Acknowledgements

The work has received partial funding from the European Union Horizon 2020 Research and Innovation Programme under Grant Agreement No. 761072 (DACOMAT).

Leonardo Di Crescenzo is acknowledged for manufacturing the specimens, and Jan Sjølin, from the Technical University of Denmark, is acknowledged for performing the experiments.

References

[1] Dugdale DS. Yielding of steel sheets containing slits. J Mech Phys Solids 1960;8:100–4.
[2] Barenblatt G. The mathematical theory of equilibrium cracks in brittle fracture. Adv Appl Mech 1962;7:55–129.
[3] Needleman A. A continuum model for void nucleation by inclusion debonding. J Appl Mech 1987;54(3):525–31.
[4] Needleman A. An analysis of tensile decohesion along an interface. J Mech Phys Solids 1990;38(3):289–324.
[5] Xu XP, Needleman A. Void nucleation by inclusion debonding in a crystal matrix. Modelling Simulation Mater Sci Eng 1993;1:111–32.
[6] Tvergaard V, Hutchinson JW. The relation between crack growth resistance and fracture process parameters in elastic-plastic solids. J Mech Phys Solids 1992;40:1377–97.
[7] Mohammed I, Liechti KM. Cohesive zone modeling of crack nucleation at bimaterial corners. J Mech Phys Solids 2000;48:735–64.
[8] Camanho PP, Davila CG, de Moura MF. Numerical simulation of mixed-mode progressive delamination in composite materials. J Compos Mater 2003;37(16):1415–38.
[9] Sørensen BF, Goutianos S, Jacobsen TK. Strength scaling of adhesive joints in polymer-matrix composites. Int J Solids Struct 2009;46:741–61.
[10] Charalambides M, Kinloch AJ, Wang Y, Williams JG. On the analysis of mixed-mode failure. Int J Fract 1992;54:269–91.
[11] Wang S, Harvey CM, Guan L. Partition of mixed modes in layered isotropic double cantilever beams with non-rigid cohesive interfaces. Eng Fract Mech 2013;111:1–25.
[12] Goutianos S, Sørensen BF. Path dependence of truss-like mixed mode cohesive laws. Eng Fract Mech 2012;91:117–32.
[13] Yang QD, Thouless MD. Mixed-mode fracture analyses of plastically-deforming adhesive joints. Int J Fract 2001;110:175–87.
[14] Park K, Paulino GH, Roesler JR. A unified potential-based cohesive model of mixed-mode fracture. J Mech Phys Solids 2009;57:891–908.
[15] Sørensen BF, Goutianos S. Mixed mode cohesive law with interface dilatation. Mech Mater 2014;70:76–93.
[16] Nguyen N, Waas AM. A novel mixed-mode cohesive formulation for crack growth analysis. Compos Struct 2016;156:253–62.
[17] Goutianos S. Derivation of path independent coupled mix mode cohesive laws from fracture resistance curves. Appl Compos Mater 2017;24(4):983–97.
[18] Tvergaard V. Effect of fibre debonding in a whisker-reinforced metal. Mater Sci Eng A 1990;125:203–13.
[19] Van den Bosch MJ, Schreurs PJG, Geers MGD. An improved description of the exponential xu and needleman cohesive zone law for mixed-mode decohesion. Eng Fract Mech 2006;73:1220–34.
[20] Jensen HM. Mixed mode interface fracture criteria. Acta Metall Mater 1990;38:2637–44.
[21] Hutchinson JW, Suo Z. Mixed mode cracking in layered materials. In: Hutchinson JW, Wu TY, editors. Advanced in applied mechanics. vol. 29, Boston: Academic Press; 1992, p. 63–191.
[22] Sørensen BF, Jacobsen TK. Characterizing delamination of fibre composites by mixed mode cohesive laws. Compos Sci Technol 2009;69:445–56.
[23] Joki RK, Grytten F, Hayman B, Sørensen BF. A mixed mode cohesive model for FRP laminates incorporating large scale bridging behaviour. Eng Fract Mech 2020;239:107274.
[24] Pappas GA, Botsis J. Variations on R-curves and traction-separation relations in DCB specimens loaded under end opening forces or pure moments. Int J Solids Struct 2020;191–192:42–55.
[25] Sørensen BF, Jørgensen K, Jacobsen TK, Østergaard RC. DCB-specimen loaded with uneven bending moments. Int J Fract 2006;141:163–76.
[26] Rice JR. A path independent integral and the approximate analysis of strain concentrations by notches and cracks. J Appl Mech 1968;35:379–86.
[27] Suo Z. Delamination specimens for orthotropic materials. J Appl Mech 1990;57:627–34.
[28] Wang SS, Mandell JF, McGarry FJ. An analysis of the crack tip stress field in DCB adhesive fracture specimens. Int J Fract 1978;14:39–58.
[29] Goutianos S. Acoustic emission characteristics of unidirectional glass/epoxy composites under mixed-mode fracture. SN Appl Sci 2019;1(5):474. http://dx.doi.org/10.1007/s42452-019-0499-z.